This is a preprint, the final version is subject to change, of the American Mineralogist (MSA)
Cite as Authors (Year) Title. American Mineralogist, in press.
(DOI will not work until issue is live.) DOI: http://dx.doi.org/10.2138/am.2013.4369

Revision1

A first principles calculation of the elastic and vibrational anomalies of lizardite under pressure

Jun Tsuchiya[1,2]

[1]Geodynamics Research Center, Ehime University, 2-5 Bunkyo-cho, Matsuyama, Ehime 790-8577 JAPAN.

[2]Earth-Life Science Institute, Ehime Satellite, 2-5 Bunkyo-cho, Matsuyama, Ehime 790-8577 JAPAN.

E-mail: junt@sci.ehime-u.ac.jp

Abstract

The crystal structure, elasticity, and vibrational properties of lizardite under pressure were determined using first principles techniques. Above 10 GPa, the stable and metastable structures were obtained. The hydrogen bond geometry of the stable structure indicates the disappearance of hydrogen bond above 10 GPa, whereas the metastable structure does not show the noticeable change of the hydrogen bond strength throughout the pressure range up to 20 GPa. At 10 GPa, a very sudden softening of the elastic constants was observed at stable structure, which is associated with a slight change in the compressibility of the c axis. This elastic softening causes a sudden reduction in the seismic velocities V_P

and V_ϕ by about 16% and 24%, respectively. These velocities, in turn, steeply increase with further compression. Shear velocity V_S, on the other hand, gradually decreases with pressure and then abruptly increases about 14% at 10 GPa. The calculated OH stretching frequencies also increase suddenly at ~10 GPa. Previous Raman measurement reported that the highest OH stretching frequencies also increase steeply above 6 GPa. Therefore, there is a possibility that this elastic anomaly can be observed experimentally at about 6 GPa.

Keywords: lizardite, first principles, elasticity, vibration, high pressure

Introduction

Serpentine is a common rock forming hydrous magnesium phyllosilicate, and it is known to form in the mantle wedge due to a reaction between peridotite and upwelling water, which is released by the decomposition of hydrous minerals in the subducting slab under pressure (e.g. Schmidt and Poli 1998, Iwamori 1998). Partially serpentinized peridotite may be a significant reservoir for hydrogen in the mantle wedge and be the convectional lubricant of subducting plates (Hilairet et al. 2007). The dehydration of serpentine is thought to contribute to the generation of arc magmatism and was also extensively investigated in connection with intermediate and deep earthquakes (e.g. Irifune et al. 1996, Dobson et al. 2002). There are three polymorphs in the serpentine group: antigorite, chrysotile, and

lizardite. Although antigorite is the most relevant mineral in these serpentine polymorphs at the subduction zone, lizardite is expected to exist in very cold regions below ~400°C (Evans 2004). Despite the geophysical and mineralogical importance of serpentine, its structural and physical properties have not been sufficiently determined. An *in situ* synchrotron X-ray diffraction study previously reported the compressibility of lizardite, antigorite, and chlysotile up to 10 GPa (Hilairet et al. 2006). Later, Nestola et al. 2009 reported the anomalous softening of antigorite at 6 GPa by single crystal X-ray diffraction. Although, Mookherjee and Stixrude (2009) reported the structure and elasticity of lizardite beyond 100 GPa, finding an elastic anomaly at 7-22 GPa, and discovering an elastic instability at 50 GPa, their data points are sparse in the vicinity of the anomaly and a more detailed calculation and analyses are needed. In this study, first principles calculations on the structural and elastic properties of lizardite up to 20 GPa, with a smaller pressure interval of less than 2 GPa were performed. In order to achieve a more detailed analysis, the vibrational properties such as the OH stretching frequencies and the Raman spectra of lizardite under pressure were also determined by using the density functional perturbation theory (DFPT).

Methods

This is a preprint, the final version is subject to change, of the American Mineralogist (MSA)
Cite as Authors (Year) Title. American Mineralogist, in press.
(DOI will not work until issue is live.) DOI: http://dx.doi.org/10.2138/am.2013.4369

First principles computations were based on the generalized gradient approximation (GGA-PBE) within the density functional theory (Hohenberg and Kohn 1964, Perdew et al. 1996). It is known that the local density approximation (LDA) overestimates the strength of the hydrogen bond and underestimates the volume, while GGA slightly overestimates the experimental volume (e.g. Lee et al. 1992, Haman 1997). Since first principles structural optimization is usually conducted at static 0 K conditions whereas the structural refinement experiments are usually conducted at ambient conditions, the difference between experiments and LDA calculations might be less if the temperature effects are included in the calculations (e.g. Stixrude, 2002). Actually, the differences in the physical properties calculated by GGA and LDA should be smaller when they are compared at the same volume, and the qualitative behaviors under pressure are usually similar between GGA and LDA (e.g. Demuth et al. 1999). In this study, GGA-PBE is employed for the elasticity calculation. The Troullier-Martins type norm conserving pseudopotentials (Troullier and Martins 1991) which were extensively tested in previous calculations (e.g. Tsuchiya and Tsuchiya, 2008, 2009) were used for this study.

The lizardite-1*T* polytype $Mg_3Si_2O_5(OH)_4$ has trigonal symmetry with the space group $P3_1m$, and the lizardite primitive cell contains 18 atoms (Mellini 1982). The electronic wave function was expanded in plane waves using a kinetic energy cutoff of 80 Ry. The

irreducible Brillouin zone of the lizardite primitive cell was sampled on a 5x5x4 Monkhorst-Pack mesh (Monkhorst and Pack 1976). All structural parameters are fully relaxed at static 0 K conditions using damped variable cell shape molecular dynamics (Wentzcovitch 1991) and the Quantum-espresso code (hppt://www.quantum-espresso.org) until residual forces became less than 1.0×10^{-5} Ry/au. The elastic constants were determined by using the stress-strain relations (Karki et al. 2001). The magnitude of all applied strains was 0.01. The linear relation was ensured for this strain range.

In order to more closely investigate the elastic anomaly which is presumably caused by the change of the hydrogen bond strength in lizardite, the vibrational properties were calculated using the linear response density functional perturbation theory (DFPT) (Baroni et al. 2001). This method has been successfully applied to investigate the vibrational properties of several hydrogen-free minerals (Tsuchiya et al. 2004a, 2004b) and a hydrous phase of AlOOH (Tsuchiya et al. 2008). The experimental IR spectrum of lizardite at ambient conditions has been excellently reproduced by using DFPT (Balan et al. 2002). For detailed comparisons with the Raman spectrum measurement (Auzende et al. 2004), the Raman intensities have been computed. The Raman tensor was computed using the second-order derivative of the electronic density matrix with respect to a uniform electric field (Lazzeri and Mauri 2003) using the phonon code implemented in Quantum-espresso.

The experimental Raman spectra of hydrous minerals have been excellently reproduced by using these calculation methods (Balan et al. 2006, Tsuchiya et al. 2008).

Results and Discussion

1. Structure

The crystal structure of lizardite consists of the SiO_4 tetrahedral layers, the MgO_6 octahedral layers, and the hydrogen bond layers. In this type of mineral, the structure is anisotropically changed by compression because it is easy to shrink along the weak direction, *i.e.* normal to the layers. Figure 1 and Table 1 show the cell constants of lizardite under pressure. Those calculated results are consistent with previous x-ray diffraction experiments (Hilairet et al. 2006a,b, Mellini and Zanazzi 1989) and previous calculation based on GGA (Mookherjee and Stixrude 2009). The length of the lizardite *a*-axis corresponds to the two basal edges of the SiO_4 tetrahedra. As mentioned above, GGA tends to overestimate the volume and underestimate the hydrogen bond strength. Since the hydrogen bond aligns along the *c*-axis in lizardite, differences between calculation and experiment are larger in the *c*-axis (~1.5%) more than the *a*-axis (~0.3%). The calculated and experimental bulk modulus are shown in Table 2. Least squares fittings of the calculated data to the third-order Birch-Murnaghan equation of state yield the zero-pressure bulk modulus B_0 of lizardite of

This is a preprint, the final version is subject to change, of the American Mineralogist (MSA)
Cite as Authors (Year) Title. American Mineralogist, in press.
(DOI will not work until issue is live.) DOI: http://dx.doi.org/10.2138/am.2013.4369

about 76.4 GPa (B'=2.39, V_0=182.3 Å^3) which is consistent with a synchrotron X-ray diffraction study (B_0=71.9 GPa, B_0'=3.2, V_0=180.92 Å^3, Hilairet et al., 2006).

The metastable structure of lizardite was also found above 10 GPa (~165 Å^3) (Figure 1-3). Note that the space group of lizardite ($P3_1m$) was maintained in both stable and metastable structures throughout the pressure range. In the stable structure, the calculated *c*-axis shows softening at about 10 GPa, whereas the metastable structure does not show such softening (Figure 1). The compression mechanism of lizardite has been stated in a previous study (Mookherjee and Stixrude 2009). In both stable and metastable structures, the volume reductions are achieved by the deformation of SiO_4 six-membered rings from hexagonal to trigonal shapes (Figure 3) in order to accommodate higher pressure conditions. However, the distortion direction of the six-membered rings is different between the stable and metastable structures (Figure 3). In the stable structure, tetrahedral rotation angle α changes from negative to positive above 10 GPa, whereas α is maintained at negative in the metastable structure (Figure 4(d)). Interestingly, those two types of distortions of SiO_4 six-membered rings have already been reported in a previous study of lizardite-*1T* and -*2H1* polytypes at ambient conditions (Mellini and Zanazzi 1987).

The hydrogen bond strength in the oxide minerals approximately correlates with the O-H···O bond angle ($\angle OH\cdots O$) and the distance between the hydrogen and two adjacent

This is a preprint, the final version is subject to change, of the American Mineralogist (MSA)
Cite as Authors (Year) Title. American Mineralogist, in press.
(DOI will not work until issue is live.) DOI: http://dx.doi.org/10.2138/am.2013.4369

123 oxygens ($R_{O\text{-}H}$ and $R_{O\cdots H}$). In general, with increasing hydrogen bond strength, the $R_{O\text{-}H}$ and
124 $R_{O\cdots H}$ bonds become longer and shorter respectively, and the hydrogen bond angle
125 $\angle OH\cdots O$ increases toward 180° (e.g Tsuchiya et al. 2005a, Tsuchiya and Tsuchiya. 2009,
126 Mookherjee and Stixrude 2009). Figure 4 shows the pressure dependence of the hydrogen
127 bond geometry of lizardite. Although the $R_{O\text{-}H}$ distances decrease in both stable and
128 metastable structures, $R_{O\cdots H}$ increases and $\angle OH\cdots O$ is noticeably decreased in the stable
129 structure whereas $R_{O\cdots H}$ decreased and $\angle OH\cdots O$ is almost constant in the metastable
130 structure above 10 GPa (Figure 4 (a-c)). Those behaviors indicate that the hydrogen bond of
131 the stable structure is almost collapsed above 10 GPa, whereas that of the metastable
132 structure is still maintained and preventing the inter-layer softening. Previous studies
133 (Nestola et al., 2010; Mookherjee and Capitani,2011) also reported the softening of the
134 *c*-axis in antigorite. Further detailed studies may be needed for the identification of the
135 mechanism that causes the softening of the c-axis in antigorite.

136 **2. Elasticity**

137 Figure 5 and Table 3 show elastic constants of lizardite under pressure. At 0 GPa,
138 C_{33} is significantly smaller than C_{11}, since C_{33} corresponds to the compressibility along the
139 *c*-axis. With increasing pressure C_{33} increases rapidly and is almost comparable to C_{11} at
140 ~10 GPa. Many of the elastic constants of lizardite show kinks at 10 GPa. Among them, C_{33}

This is a preprint, the final version is subject to change, of the American Mineralogist (MSA)
Cite as Authors (Year) Title. American Mineralogist, in press.
(DOI will not work until issue is live.) DOI: http://dx.doi.org/10.2138/am.2013.4369

and C_{13} show the most striking change. These changes can be explained by the disappearance of hydrogen bonds and softening of the *c*-axis as shown in Figure 1 and 4. Shear elastic constants C_{44} and C_{66} show almost no pressure dependence up to 10 GPa, then C_{44} shows a step-like increase at 10 GPa (Figure5(c)). In contrast, C_{66} is not affected by the softening of the *c*-axis, since C_{66} is the elastic constant related to the shearing of the layer and is of no relevance to the softening of the *c*-axis. Huge drops of C_{33} and C_{13} are somewhat counter-intuitive since the hydrogen bond which is aligning along *c*-axis in lizardite is attractive force and the disappearance of hydrogen bond leads to the softening of the layers. However, the present results indicate that the disappearance of hydrogen bonds induces the close-fitting between the layers of lizardite under pressure.

A study by Mookherjee and Stixrude (2009) reported an elastic anomaly of lizardite where several elastic constants decrease with pressure at 7-22 GPa. The overall behavior of the elastic anomaly in this study is consistent with the study by Mookherjee and Stixrude (2009). However, in the present study, the elastic constants decrease more severely at 10 GPa and the pressure range where the elastic constants decrease is more localized within a small pressure interval of only a few GPa.

Bulk and shear moduli determined by the Voigt, Ruess, and Hill averages are shown in Figure 6(a). The bulk modulus increases with pressure and suddenly drops above

This is a preprint, the final version is subject to change, of the American Mineralogist (MSA)
Cite as Authors (Year) Title. American Mineralogist, in press.
(DOI will not work until issue is live.) DOI: http://dx.doi.org/10.2138/am.2013.4369

10 GPa because of an anomalous drop of the elastic constants. The shear modulus of lizardite shows almost no pressure dependence except for the elevation at 10 GPa associated with the C_{44} shear elastic constants anomaly. The differences of these moduli between Voigt and Reuss limits at 0 GPa are very large, which reflects the very anisotropic crystal structure of serpentine (Figure 6(a)). With increasing pressure, the difference in the bulk modulus between the Voigt and Reuss averages (B_V and B_R) decreases rapidly whereas the difference between G_V and G_R is almost unchanged.

Figure 6(b) shows the velocities of lizardite under pressure. This elastic softening causes a reduction in seismic velocities V_P and V_ϕ by about 16% and 24%, respectively. These velocities, in turn, suddenly increase with further compression. Shear velocity V_S, on the other hand, gradually decreases with pressure and then abruptly increases about 14% at 10 GPa. Since these valley- and step-like changes in velocities complete within very small pressure intervals (2-3 GPa), previous investigations may have failed to detect these elastic anomalies.

3. Born stability criteria

If a crystal is mechanically stable, the elastic wave energy is positive and the elastic constant matrix should be positive definite. This is known as the Born stability criteria (Born

This is a preprint, the final version is subject to change, of the American Mineralogist (MSA)
Cite as Authors (Year) Title. American Mineralogist, in press.
(DOI will not work until issue is live.) DOI: http://dx.doi.org/10.2138/am.2013.4369

and Huang, 1954). In order to check the mechanical stability of lizardite, the Born stability criteria was calculated under pressure. The Born stability criteria for a trigonal system are,

$B_1 = C_{11} - |C_{12}| > 0$, (1)

$B_2 = (C_{11} + C_{12})C_{33} - 2C_{21}^3 > 0$, (2)

$B_3 = (C_{11} - C_{12})C_{44} - 2C_{21}^4 > 0$. (3)

As shown in Figure 7, B_1, B_2, and B_3 are positively defined, even though a sudden drop of the elastic constants at 10 GPa occurred. Although the pressure of this anomaly is higher than the stability field of lizardite, these results suggest that lizardite is still mechanically stable. Therefore, there is a possibility that this elastic anomaly can be observed experimentally if it is metastably compressed and carefully measured with sufficiently small pressure intervals.

4. Vibrational property

In order to further inspect the hydrogen bond characteristic of lizardite, the vibrational properties of lizardite under pressure are calculated based on DFPT. Though, DFPT calculations of anhydrous systems have been shown to successfully describe their vibrational properties (e.g. Tsuchiya et al. 2005b), that of a hydrogen bonded system has been reported to be associated with larger calculation errors (Tsuchiya and Tsuchiya 2008). Therefore, DFPT calculations using two different electron exchange and correlation

functionals were performed: GGA and LDA in order to the grasp the general trends of two functionals, the range of errors, and the qualitative behavior of vibrational properties under pressure. Figure 8 shows the OH stretching frequencies of lizardite under pressure. Eventually, the experimental OH stretching frequencies were found between the calculated frequencies using LDA and GGA.

The experimental vibrational frequencies and Infrared and Raman spectrum of lizardite at ambient conditions have been reported in previous studies (Balan et al. 2002, Hofmeister and Bowey 2006, Post and Borer 2000, Fuchs et al. 1998, Rinaudo et al. 2003). The normal modes, IR spectrum, and their peak assignments of lizardite at ambient conditions are extensively discussed and clarified in previous studies (Balan et al. 2002, Prencipe et al. 2009). The vibrational frequency pressure dependence of lizardite has been reported by a Raman spectroscopic measurement (Auzende et al., 2004). They reported that there are two sets of the OH stretching frequencies, one with a shallower and another is steeper slopes under pressure as shown in Figure 8.

The calculated OH stretching frequencies gradually decrease at lower pressures and then suddenly increase at pressures above ~10 GPa (Figure 8). Those behaviors are closely correlated with the O-H bond geometry as shown in Figure 4. The abrupt increase of OH stretching frequencies above 10 GPa can therefore be explained by the disappearance of

hydrogen bond. There is no calculated vibrational mode whose frequency has steadily increasing with pressure as reported in the previous experiment. Considering the experimental difficulty of the assignment of vibrational modes and experimental errors for the determination of the vibrational peak positions, there is a possibility that the experimental O-H vibrations can also be interpreted by the shallower slopes at lower pressure condition below ~6 GPa and steeper slopes at higher pressure condition above 6 GPa.

It has been pointed out that the vibrational frequencies can be influenced by the coupling of atomic vibrations with a macroscopic electric field (LO-TO splitting) and therefore vibrational frequencies depend on the macroscopic shape of the measured particles (Balan et al. 2006). In a common spectroscopic experimental setting, the samples were polycrystalline material which was typically larger than a few 100 nm in size. In such coarse polycrystalline grains, both LO and TO modes can be measured by Raman spectroscopic measurements (Farmer 2000). Figure 9 shows the theoretical Raman cross section of lizardite under pressure. Several OH peaks have previously been observed experimentally presumably because they used natural samples which contain impurities. The calculated Raman spectra show that the most intense peaks are existing around 3730 cm^{-1} (LO) and 3770 cm^{-1} (TO) at below 10 GPa and the frequencies of those peaks rapidly increase above

This is a preprint, the final version is subject to change, of the American Mineralogist (MSA)
Cite as Authors (Year) Title. American Mineralogist, in press.
(DOI will not work until issue is live.) DOI: http://dx.doi.org/10.2138/am.2013.4369

10 GPa. Experimental results show a similar increase of OH frequencies at pressures above ~6 GPa, though those vibrational modes were fitted with a straight line throughout the pressure range previously measured (Figure 8). Since the experimental frequencies overlap and peak positions are not clear at lower pressure conditions, there is a possibility that the increase in vibrational frequencies is associated with the elastic anomaly found in this study. In that case, the elastic anomaly, which occurs at ~10 GPa (GGA) in the present study, may be observed experimentally at lower pressures of about 6 GPa in experiments. There is a similar report that the OH vibrational frequencies of layered hydrous minerals rapidly increase due to a phase transition under pressure (Johnston et al. 2002). Therefore, there is a possibility that other layered hydrous minerals show similar behaviors under compression.

Conclusions

The structure, elasticity, and vibrational properties of lizardite have been determined by first principles density functional calculations. At 10 GPa, elastic constants dropped very suddenly and are associated with the softening of the *c* axis. The OH stretching frequencies also increase steeply above 10 GPa. Since experimental results show a similar increase in frequencies at pressures above ~6 GPa, there is a possibility that this elastic anomaly can also be observed at ~6 GPa. Since elastic softening of lizardite is associated

249 with the ditrigonal distortion of SiO_4 six-membered rings, there is a possibility that other
250 hydrous sheet silicates show similar elastic and vibrational anomalies under pressure.

251 **Acknowledgements**

252 Research supported in part by special coordination funds for promoting science and
253 technology (Supporting Young Researchers with Fixed-term Appointments) and
254 Grants-In-Aid for Scientific Research from the Japan Society (Nos. 21740380, 20103005,
255 and 24740357) for the Promotion of Science. The crystal structural image of Figure 3 was
256 drawn using VESTA, developed by Momma and Izumi (2011).
257

References cited

Auzende, A.-L., Daniel, I., Reynard, B., Lemaire, C., and Guyot, F. (2004) High-pressure behaviour of serpentine minerals: a Raman spectroscopic study, Physics and Chemistry of Minerals, 31, 269-277.

Balan, E., Lazzeri, M., Morin, G., and Mauri, F. (2006) First-principles study of the OH-stretching modes of gibbsite, American Mineralogist, 91, 115-119.

Balan, E., Saitta, A. M. Mauri, F., Lemaire, C., and François, G. (2002) First-principles calculation of the infrared spectrum of lizardite, American Mineralogist, 87, 1286-1290.

Baroni, S., de Gironcoli, S., Dal Corso, A., and Giannozzi, P. (2001) Phonons and related crystal properties from density-functional perturbation theory, Review of Modern Physics, 73, 515-562.

Born, M. and Huang, K. (1954) Dynamical theory of crystal lattices, Oxford University Press, Oxford.

Demuth, Th., Jeanvoine, Y., Hafner, J., and Ángyán, J. G. (1999) Polymorphism in silica studies in the local density and generalized-gradient approximations, Journal of Physics: Condensed Matter, 11, 3833-3874.

Dobson, D. P., Meredith, P. G., and Boon, S. A., (2002) Simulation of subduction zone seismicity by dehydration of serpentine, Science, 298, 1407-1410.

Evans, B.W. (2004) The serpentine multisystem revisited: chrysotile is metastable,

277 International Geology Review, 46, 479-506.

278 Farmer, V. C. (2000) Transverse and longitudinal crystal modes associated with OH
279 stretching vibrations in single crystals of kaolinite and dickite, Spectrochim Acta Part A, 56,
280 927-930.

281 Fuchs, Y., Linares, J., and Mellini, M. (1998) Mössbauer and infrared spectrometry of
282 lizardite-1*T* from Monte Fico, Elba, Physics and Chemistry of Minerals, 26, 111-115.

283 Hamann, D. R. (1997) H_2O hydrogen bonding in density-functional theory, Physical Review
284 B, 55, R10157-R10160.

285 Hilairet, N., Daniel, I., and Raynard, B. (2006) P-V equation of state and the relative
286 stabilities of serpentine varieties, Physics and Chemistry of Minerals, 33, 629-637.

287 Hilairet, N., Reynard, B., Wang, Y., Daniel, I., Merkel, S., Nishiyama, N., and Petitgirard, S.
288 (2007) High-Pressure Creep of Serpentine, Interseismic Deformation, and Initiation of
289 Subduction, Science, 318, 1910-1973.

290 Hofmeister, A.M., and Bowey, J.E. (2006) Quantitative infrared spectra of hydrosilicates and
291 related minerals, Monthly Notices of the Royal Astronomical Society, 367, 577-591.

292 Hohenberg, P. and Kohn, W. (1964) Inhomogeneous electron gas, Physical Review, 136,
293 B864-B871.

294 Irifune, T., Kuroda, K., Funamori, N., Uchida, T., Yagi, T., Inoue, T., and Miyajima, N.

295 (1996) Amorphization of Serpentine at High Pressure and High Temperature, Science, 272,
296 1468-1470.
297 Iwamori, H. (1998) Transportation of H_2O and melting in subductionzones, Earth and
298 Planetary Science Letters, 160, 65-80.
299 Johnston, C. T., Wang, S. L., Bish, D. L., Dera, P., Agnew, S. F., and Kenney III, J. W.
300 (2002) Novel pressure-induced phase transformations in hydrous layered materials,
301 Geophysical Researcg Letters, 29, 1770.
302 Karki, B. B., Stixrude, L., and Wentzcovitch, R. M. (2001) High-pressure elastic properties
303 of major materials of earth's mantle from first principles, Reviews of Geophysics, 39,
304 507-534.
305 Lazzeri, M. and Mauri, F. (2003) First-Principles Calculation of Vibrational Raman Spectra
306 in Large Systems: Signature of Small Rings in Crystalline SiO_2, Physical Review Letters, 90,
307 036401.
308 Lee, C., Vanderbilt, D., Laasonen, K., Car, R., and Parrinello, M. (1992) Ab initio studies on
309 high pressure phases of ice, Physical Review Letters, 69, 462-465.
310 Mellini, M. (1982) The crystal structure of lizardite *1T*: hydrogen bonds and polytypism,
311 American Mineralogist, 67, 587-598.
312 Mellini, M. and Zanazzi, P. F. (1987) Crystal structures of lizardite-*1T* and lizardite-*2H1*

313 from Coli, Italy, American Mineralogist, 72, 943-948.

314 Mellini, M. and Zanazzi, P. F. (1989) Effects of pressure on the structure of lizardite-1*T*,

315 European Journal of Mineralogy, 1, 13-19.

316 Monkhorst, H. J. and Pack, J. D. (1976) Special points for Brillouin-zone integrations,

317 Physical Review B, 13, 5188-5192.

318 Momma, K. and Izumi, F. (2011) VESTA 3 for three-dimensional visualization of crystal,

319 volumetric and morphology data, Journal of Applied Crystallography, 44, 1272-1276.

320 Mookherjee, M. and Capitani, G. C. (2011) Trench parallel anisotropy and large delay times:

321 Elasticity and anisotropy of antigorite at high pressures, Geophysical Research Letters, 38,

322 L09315.

323 Mookherjee, M. and Stixrude, L. (2009) Structure and elasticity of serpentine at

324 high-pressure, Earth and Planetary Science Letters, 279, 11-19.

325 Nestola, F., Angel, R. J., Zhao, J., Garrido, C. J., Sánchez-Vizcaíno, V. L., Capitani, G., and

326 Mellini, M. (2010) Antigorite equation of state and anomalous softening at 6 GPa: an in situ

327 single-crystal X-ray diffraction study, Contributions to Mineralogy and Petrology, 160,

328 33-43.

329 Perdew, J. P., Burke, K., and Ernzerhof, M. (1996) Generalized Gradient Approximation

330 Made Simple, Physical Review Letters, 77, 3865-3868.

331 Prencipe, M., Noel, Y., Bruno, M., and Dovesi, R. (2009). The vibrational spectrum of
332 lizardite-*1T* [$Mg_3Si_2O_5(OH)_4$] at the G point: a contribution from an ab initio periodic
333 B3LYP calculation, American Mineralogist, 94, 986-994.
334 Post, J.L. and Borer, L. (2000) High-resolution infrared spectra, physical properties, and
335 micromorphology of serpentines, Applied Clay Science, 16, 73-85.
336 Rinaudo, C., Gastaldi, D. and Belluso, E. (2003) Characterization fo chrysotile, antigorite,
337 and lizardite by FT-Raman Spectroscopy, Canadian Mineralogist, 41, 883-890.
338 Schmidt, M. W. and Poli, S. (1998) Experimentally based water budgets for dehydrating
339 slabs and consequences for arc magma generation, Earth and Planetary Science Letters, 163,
340 361-379.
341 Stixrude, L. (2002) Talc under tension and compression: Spinodal instability, elasticity, and
342 structure, Journal of Geophysical Research, 107, 2327.
343 Troullier, N. and Martins, J. L. (1991) Efficient pseudopotentials for plane-wave calculations,
344 Physical Review B, 43, 1993-2006.
345 Tsuchiya, J., and Tsuchiya, T. (2008) Elastic properties of phase D ($MgSi_2O_6H_2$) under
346 pressure: Ab initio investigation, Physics of the Earth and Planetary Interiors, 170, 215-220.
347 Tsuchiya, J. and Tsuchiya, T. (2009) First principles investigation of the structural and
348 elastic properties of hydrous wadsleyite under pressure, Journal of Geophysical Research,

114, B02206.

Tsuchiya, J., Tsuchiya, T., and Tsuneyuki, S. (2005a) First-principles study of hydrogen bond symmetrization fo phase D under high pressure, American Mineralogist, 90, 44-49.

Tsuchiya, J., Tsuchiya, T., and Wentzcovitch, R. M. (2005b) Vibrational and thermodynamics properties of $MgSiO_3$ postperovskite, Journal of Geophysical Research, 110, B02204.

Tsuchiya, J., Tsuchiya, T., and Wentzcovitch, R. M. (2008) Vibrational properties of δ-AlOOH under pressure, American Mineralogist, 93, 477-482.

Tsuchiya, T., Caracas, R., and Tsuchiya, J. (2004a) First principles determination of the phase boundaries of high-pressure polymorphs of silica, Geophysical Research Letters, 31, L11610.

Tsuchiya, T., Tsuchiya, J., Umemoto, K., and Wentzcovitch, R. M. (2004b) Phase transition in $MgSiO_3$ perovskite in the Earth's lower mantle, Earth and Planetary Science Letters, 224, 241-248.

Wentzcovitch, R. M. (1991) Invariant molecular-dynamics approach to structural phase transitions, Physical Review B, 44, 2358-2361.

368
369
370 **Figure Captions**

371 **Figure 1.** Calculated and experimental cell parameters of lizardite. Full and dashed lines
372 are calculated results of the stable and metastable structure of lizardite, respectively. The
373 open circle and triangle are experimental results (Hilairet et al. 2006, Mellini and Zanazzi
374 1989).

375 **Figure 2.** Enthalpy difference between the stable and metastable structures of lizardite.

376 **Figure 3.** Crystal structure of lizardite ($Mg_3Si_2O_9H_4$) at 0 and 14 GPa. Blue tetrahedra,
377 and orange octahedra correspond to SiO_4 and MgO_6, respectively. Large (orange), middle
378 (blue), small (red), very small (white) spheres are magnesium, silicon, oxygen, and
379 hydrogen, respectively. The green arrows on the high pressure structures correspond to the
380 direction of distortion of the SiO_4 six-membered rings under pressure.

381 **Figure 4** The calculated (a) O-H bond distances $R_{O\text{-}H}$, (b) the hydrogen bond distances
382 $R_{O\ldots H}$ (c) the O-H…O angles, and (d) the tetrahedral rotation angle α of lizardite under
383 pressure. The full and dashed lines are stable and metastable structures, respectively. The
384 gray lines indicate the $R_{O\text{-}H}$ in the tetrahedral layers.

385 **Figure 5** High pressure elastic constants of lizardite.

386 **Figure 6** (a) Bulk and shear moduli and (b) velocities of lizardite under pressure. Upper
387 and lower thin lines are Voigt and Reuss bounds, respectively.

388 **Figure 7** Born stability criteria (B_1, B_2, and B_3) of lizardite under pressure.

389 **Figure 8** Vibrational frequencies of lizardite under pressure.

390 **Figure 9** Raman cross section of lizardite under pressure using GGA. Convolution with a
391 Lorentzian function with a full width at half height of 10 cm^{-1} was used to account for the
392 broadening of experimental peaks. Inset shows the experimental Raman spectra of
393 lizardite under pressure (Auzende et al. 2004).

394

395

Table1 Calculated cell constants and atomic coordinates of lizardite under pressure.

P (GPa)	a(Å)	c (Å)	Mg_x	Mg_z	Si_z	$O1_z$	$O2_x$	$O2_z$	$O3_y$	$O3_z$	$O4_z$	$H1_x$	$H1_z$	$H2_z$
0	5.345	7.403	0.331	0.458	0.080	0.297	0.511	0.998	0.664	0.590	0.309	0.651	0.720	0.178
2	5.316	7.239	0.331	0.460	0.075	0.295	0.514	0.990	0.665	0.594	0.304	0.650	0.727	0.171
4	5.288	7.130	0.331	0.461	0.072	0.295	0.517	0.986	0.665	0.596	0.301	0.650	0.732	0.166
6	5.263	7.050	0.331	0.463	0.071	0.296	0.519	0.983	0.666	0.599	0.299	0.650	0.736	0.162
8	5.239	6.990	0.331	0.463	0.070	0.296	0.523	0.981	0.667	0.600	0.296	0.651	0.738	0.158
10	5.223	6.904	0.331	0.462	0.067	0.296	0.495	0.976	0.668	0.601	0.292	0.649	0.740	0.152
12	5.190	6.828	0.331	0.462	0.064	0.295	0.466	0.972	0.668	0.602	0.289	0.649	0.743	0.148
14	5.157	6.773	0.331	0.463	0.063	0.295	0.451	0.971	0.668	0.605	0.288	0.651	0.746	0.146
16	5.129	6.724	0.331	0.464	0.061	0.295	0.441	0.970	0.668	0.606	0.287	0.654	0.748	0.144
18	5.101	6.679	0.331	0.463	0.059	0.295	0.432	0.968	0.669	0.607	0.286	0.659	0.750	0.141
20	5.074	6.636	0.331	0.464	0.058	0.294	0.425	0.967	0.669	0.609	0.284	0.665	0.753	0.139
Exp[1]														
0	5.332	7.233	0.3327	0.4596	0.0766	0.300	0.5087	0.9964	0.6654	0.5935	0.3088	0.6550	0.709	0.199

Si_x=1/3, Si_y=2/3, $O1_x$=1/3, $O1_y$=2/3

[1]Mellini (1982),

Table 2 Calculated and experimental equation of state parameters of lizardite.

V (Å^3)	B_0 (GPa)	B_0'	
182.3	76.4	2.39	Calc. GGA, 0 K (present study)
186.34	41.36	12.38	Calc. GGA 0 K[a] (< 7 GPa)
203.15	35.64	4.09	Calc. GGA 0 K[a] (7<P<22 GPa)
170.76	79.93	12.34	Calc. LDA 0 K[a] (< 7 GPa)
173.52	74.61	3.10	Calc. LDA 0 K[a] (7<P<22 GPa)
174.02	61.05	17.25	Calc. LDA 300 K[a] (<7 GPa)
180.93	68.9	4 (fixed)	Exp. Synchrotron x-ray diffraction 300 K[b]
180.92	71.0	3.2	Exp. Synchrotron x-ray diffraction at 300 K[b]

[a] Mookherjee and Stixrude 2009.

[b] Hilairet et al. 2006

Table3. The elastic constants of lizardite.

Pressure (GPa)	C_{11}	C_{33}	C_{12}	C_{13}	C_{14}	C_{44}	C_{66}
0	212.6	57.3	73.3	8.5	1.3	11.6	69.7
2	222.1	102.0	78.5	21.6	1.7	13.4	71.9
4	228.4	133.6	82.1	34.5	1.6	13.5	73.5
6	231.2	159.4	81.8	48.1	1.9	12.6	74.7
8	229.8	178.3	78.8	62.9	1.7	11.2	75.7
9	227.7	185.8	76.2	71.0	1.2	9.9	76.1
10	223.7	195.4	71.5	77.6	1.3	8.2	76.1
10.5	216.1	119.6	62.8	0	2.1	8.2	76.7
11	209.5	106.7	56.0	14.3	2.6	14.5	76.8
11.5	210.6	184.3	57.3	22.0	2.6	14.8	76.7
12	213.4	194.8	59.8	27.3	2.8	15.7	76.8
14	219.8	204.5	67.1	39.3	2.2	15.3	77.1
16	225.8	214.9	74.1	46.8	2.4	14.9	77.0
18	229.3	221.0	79.9	51.0	2.9	13.1	76.5
20	229.6	220.9	84.2	50.3	5.7	10.3	75.7

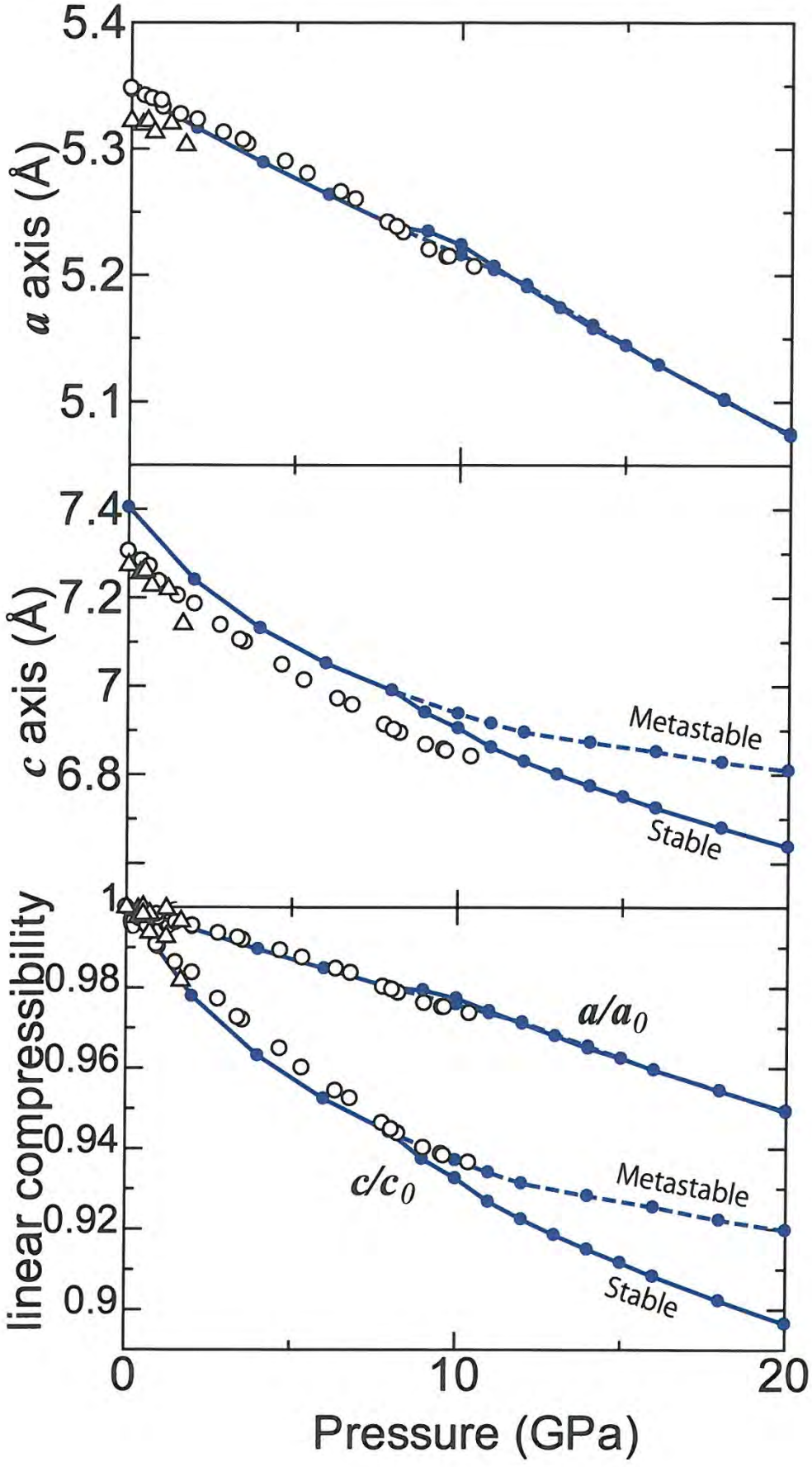
5.4
5.3
5.2
5.1
a axis (Å)
7.4
7.2
7
6.8
c axis (Å)
Metastable
Stable
1
0.98
0.96
0.94
0.92
0.9
linear compressibility
a/a0
c/c0
Metastable
Stable
0
10
20
Pressure (GPa)

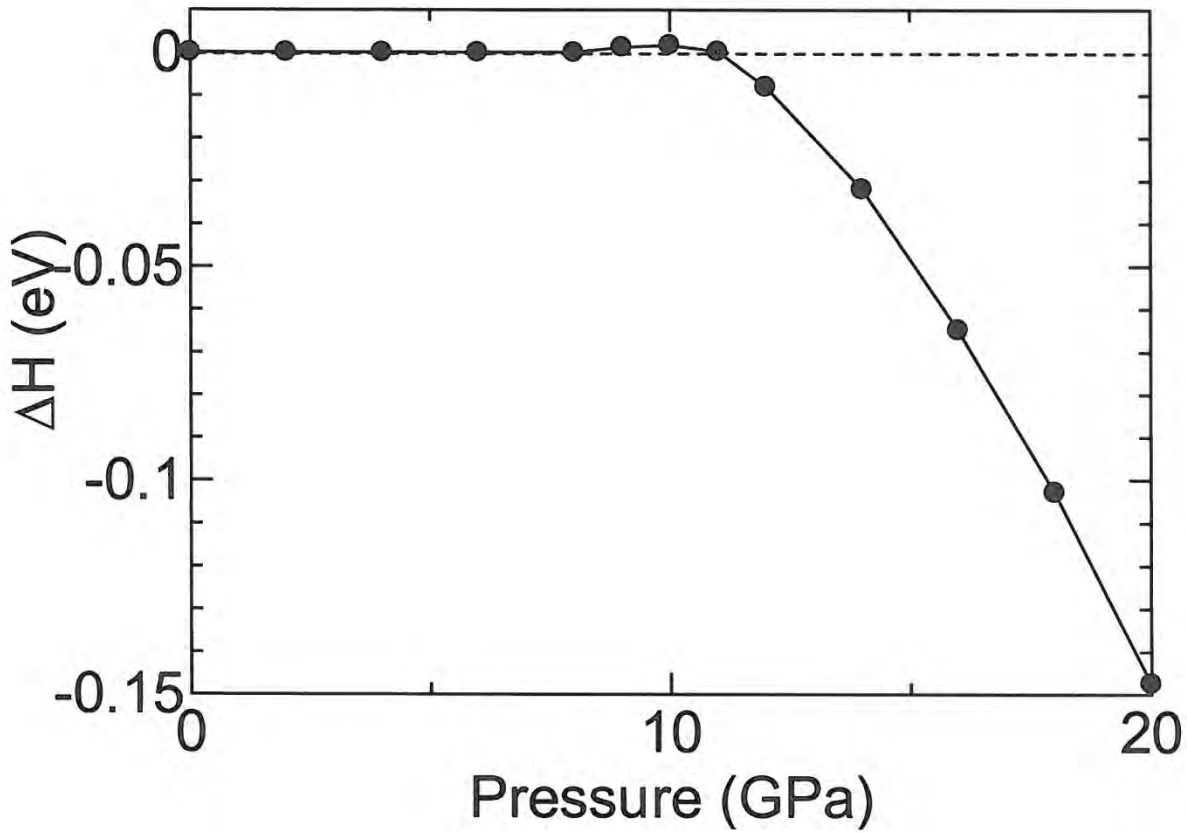
0
-0.05
-0.1
-0.15
ΔH (eV)
0
10
20
Pressure (GPa)

Stable structure (0 GPa)

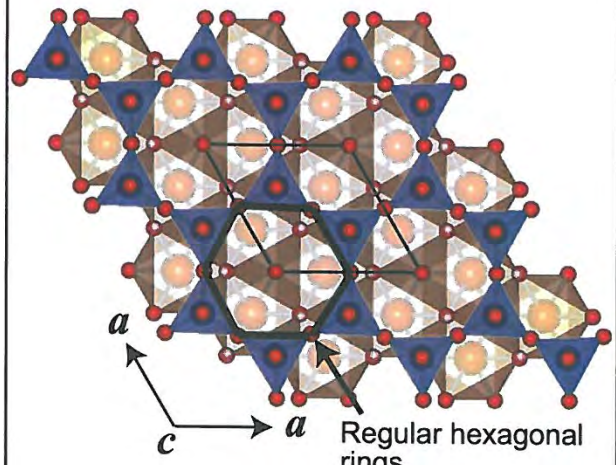

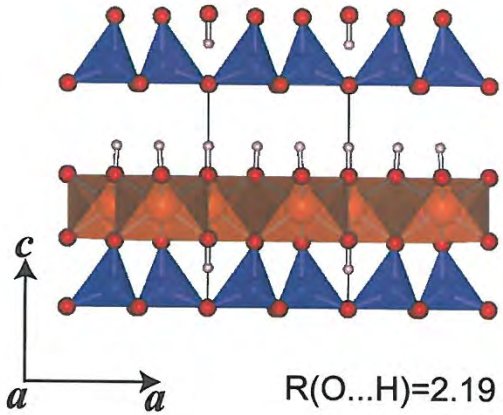

R(O...H)=2.19 Å
R(OH)=0.968 Å
∠OH...O~164°

Stable structure (14 GPa)

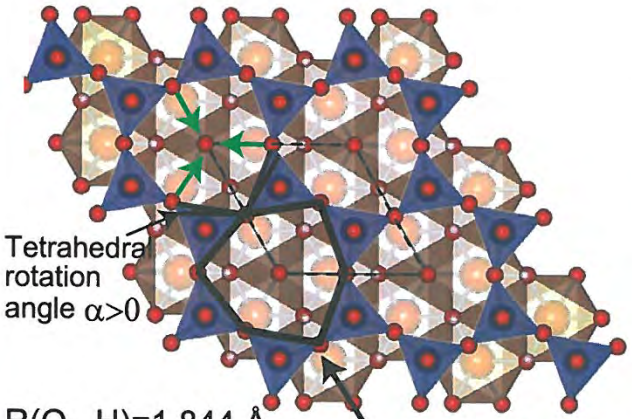

R(O...H)=1.844 Å
R(OH)=0.965 Å
∠OH...O~151°

Metastable structure (14 GPa)

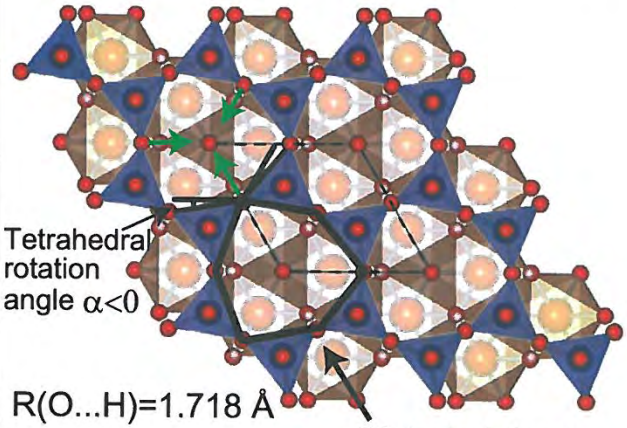

R(O...H)=1.718 Å
R(OH)=0.965 Å
∠OH...O~164°

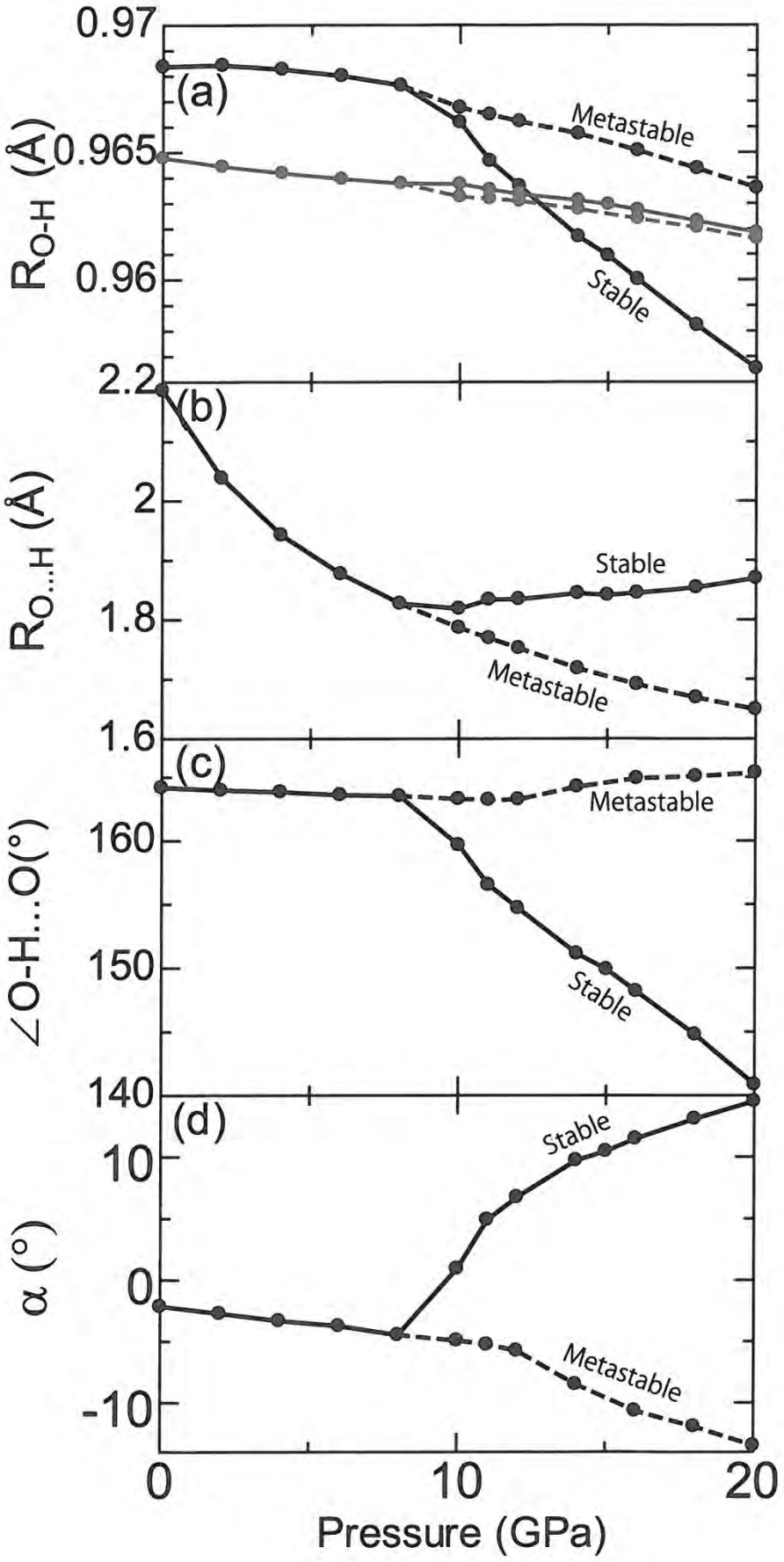
0.97
0.965
0.96
(a)
Metastable
Stable
R_{O-H} (Å)
2.2
2
1.8
1.6
(b)
Stable
Metastable
$R_{O...H}$ (Å)
160
150
140
(c)
Metastable
Stable
∠O-H...O(°)
10
0
-10
(d)
Stable
Metastable
α (°)
0
10
20
Pressure (GPa)

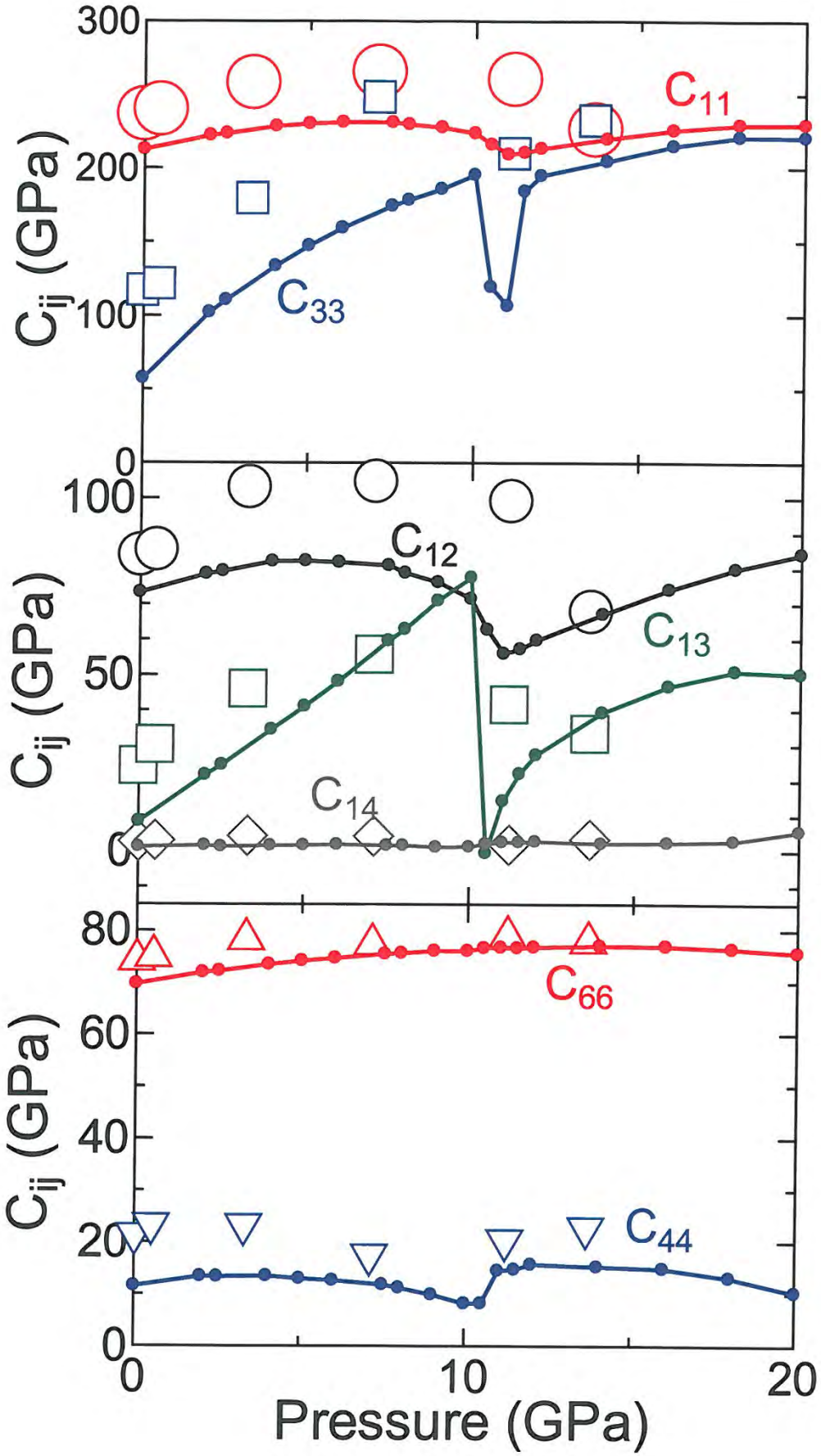
300
200
100
0
C_{ij} (GPa)
C_{11}
C_{33}
100
50
0
C_{ij} (GPa)
C_{12}
C_{13}
C_{14}
80
60
40
20
0
C_{ij} (GPa)
C_{66}
C_{44}
0
10
20
Pressure (GPa)

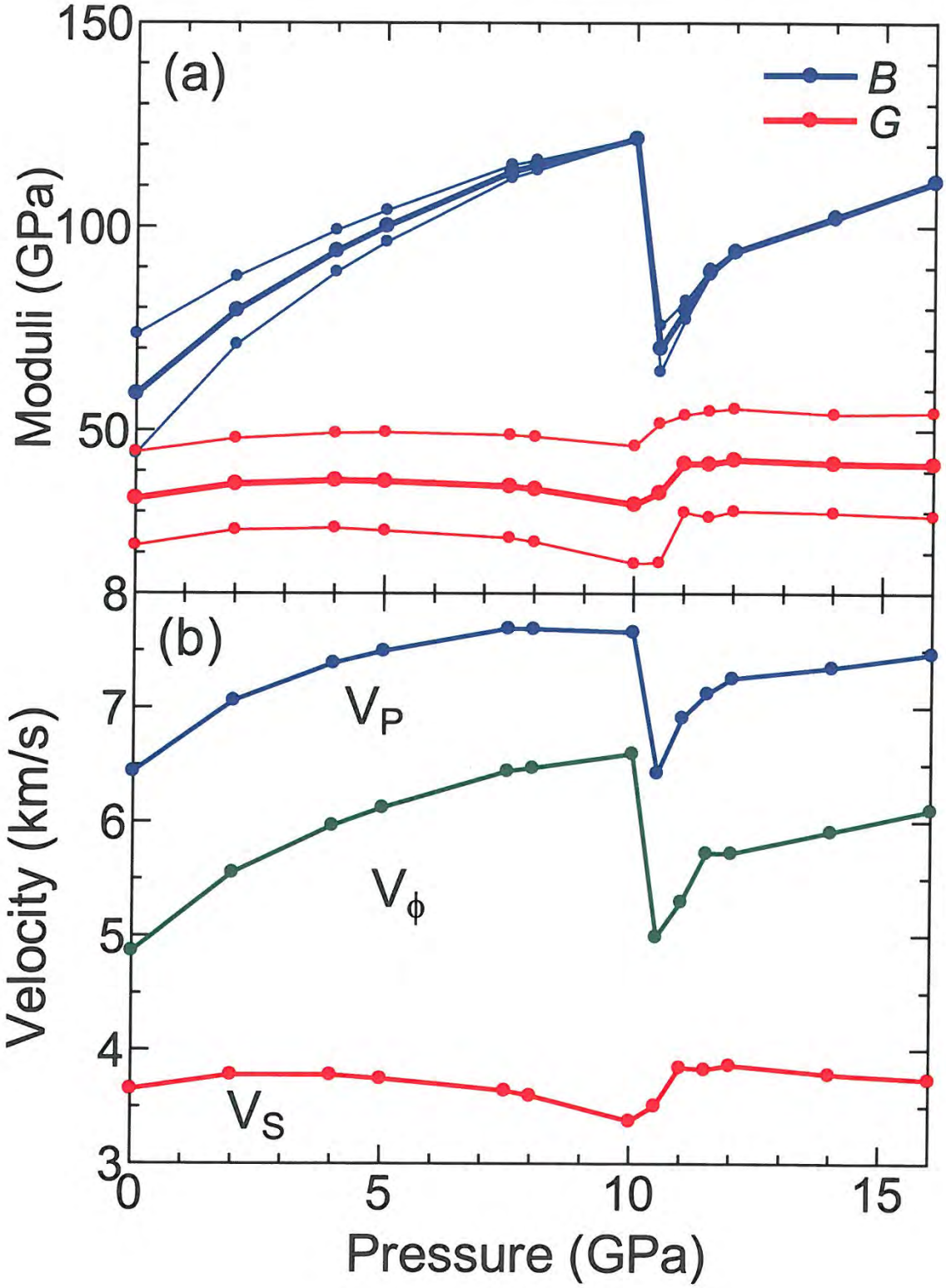
(a)
B
G
Moduli (GPa)
150
100
50
8
(b)
V_P
V_ϕ
V_S
Velocity (km/s)
7
6
5
4
3
0
5
10
15
Pressure (GPa)

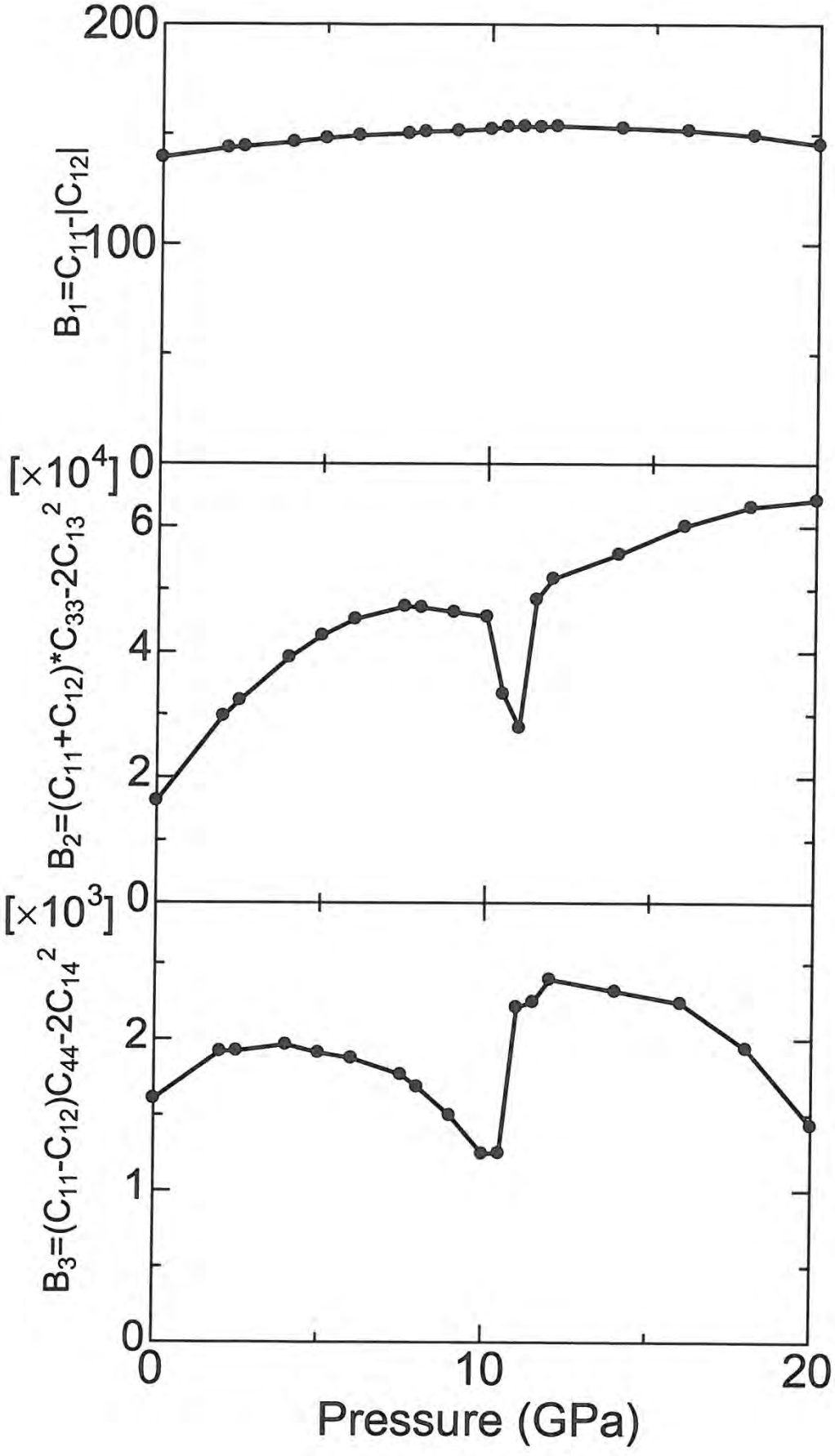
200
100
0
$B_1=C_{11}-|C_{12}|$
$[\times 10^4]$
6
4
2
0
$B_2=(C_{11}+C_{12})*C_{33}-2C_{13}^2$
$[\times 10^3]$
2
1
0
$B_3=(C_{11}-C_{12})C_{44}-2C_{14}^2$
0
10
20
Pressure (GPa)

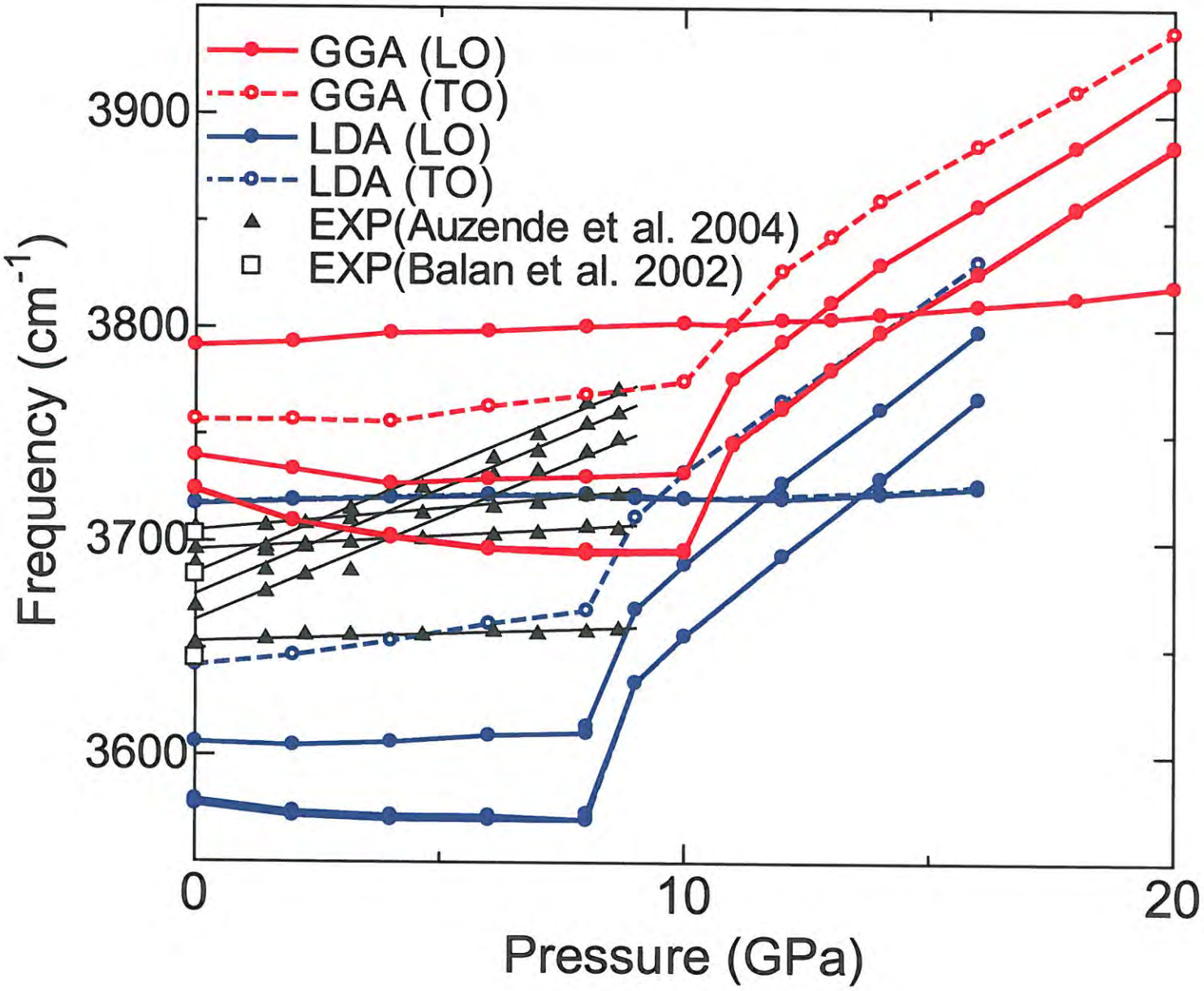
GGA (LO)
GGA (TO)
LDA (LO)
LDA (TO)
EXP(Auzende et al. 2004)
EXP(Balan et al. 2002)
3900
3800
3700
3600
Frequency (cm-1)
0
10
20
Pressure (GPa)

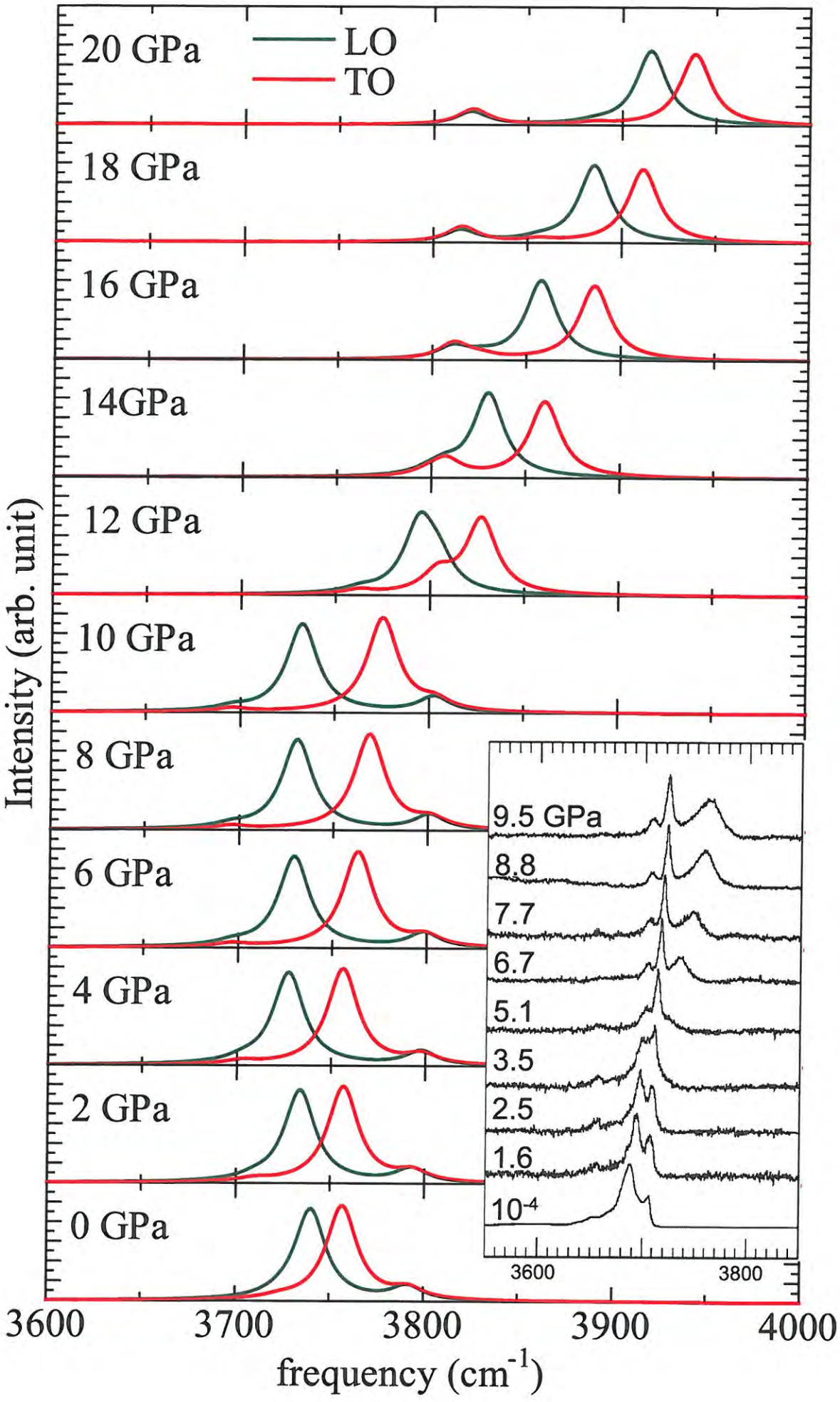
20 GPa
LO
TO
18 GPa
16 GPa
14GPa
12 GPa
10 GPa
8 GPa
6 GPa
4 GPa
2 GPa
0 GPa
9.5 GPa
8.8
7.7
6.7
5.1
3.5
2.5
1.6
10-4
3600
3800
Intensity (arb. unit)
3600
3700
3800
3900
4000
frequency (cm-1)